RESEARCH ARTICLE

BON VIEW PUBLISHING

An Improved Computational Model Based on Cardiac Imaging Data for the Quantitative and Qualitative Assessment of the Mechanical Properties of the Human Left Ventricle

Rania Awadi[1] , Narjes Benameur[1], Wafa Baccouch[1] , Mohamed Deriche[2,*] , Arnab Palit[3] , Moncef Aloui[4] ,
Nadjia Kachenoura[5] and Salam Labidi[1]

[1] *Laboratory of Biophysics and Medical Technologies, University of Tunis El Manar, Tunisia*

[2] *Artificial Intelligence Research Centre, Ajman University, United Arab Emirates*

[3] *Warwick Manufacturing Group, The University of Warwick, UK*

[4] *Military Hospital of Tunis, University of Tunis El Manar, Tunisia*

[5] *Laboratoire d'Imagerie Biomédicale, Sorbonne Université, France*

Abstract: Computational modeling has contributed to many fields of medicine and has been proven very useful for diagnosing complex diseases. A special case is that of myocardial infarction (MI), a prevalent cardiovascular disease where computational modeling approaches have been useful for detecting abnormalities. The aim of this paper is to propose enhanced computational models for the human left ventricle (LV) to estimate the strain and stress distributions in healthy and diseased subjects. Computational models were developed and evaluated using human LV of 20 patients with MI and 20 healthy controls using cardiac magnetic resonance imaging acquisitions and simulation tools. The finite element technique was employed for LV modeling. Comparative analysis revealed higher global strains in healthy subjects compared to MI patients, particularly global circumferential, longitudinal, and radial strains. The average stress distributions were 67.9 ± 5.01 kPa in healthy models and 78.3 ± 8.21 kPa in infarcted regions. Model-derived strain data indicated an overall average of -0.15 ± 0.06 for healthy models and 0.2 ± 0.04 for infarcted regions. LV strain values were compared with those obtained from two feature-tracking algorithms to validate the proposed models, resulting in very promising findings. The work presented here highlights the importance of computational modeling for quantitative and qualitative analyses of heart disease and the potential of using such models in other organs. When combined with imaging data, the proposed models can have significant implications for improved patient care and treatment strategies.

Keywords: left ventricle, modeling, finite element, strain, cardiac magnetic resonance imaging, simulation

1. Introduction

Cardiovascular diseases are the leading cause of mortality worldwide and a major contributor to disability [1]. The majority of cardiovascular disease-related deaths result from heart failure, stroke, and coronary artery disease [2]. Among this, myocardial infarction (MI) is one of the most common outcomes [3, 4]. Post-MI remodeling can alter the mechanical properties of the myocardium and cardiac muscle, potentially leading to heart failure [5]. Studies have shown that post-MI remodeling involves structural and functional changes in the heart, including alterations in size, shape, myocardial composition, contractility, and stiffness [6, 7].

Cardio-radiology relies on the accurate analysis of electrocardiograms, invasive or computed tomography coronary angiograms, and magnetic resonance imaging (MRI) data for the diagnosis and treatment of patients with MI [8–11]. Although they are essential for detecting abnormalities, they offer no information regarding the mechanical properties of the altered myocardium and its remodeling process [12].

Computational modeling, particularly through the finite element (FE) method, is a powerful approach for solving complex physical problems governed by partial differential equations. By discretizing a system into smaller, manageable elements, the FE method enables the analysis of intricate geometries, material behaviors, and multiphysics interactions that are often intractable analytically. In cardiology, its utility is significantly enhanced when it is integrated with imaging techniques such as cardiac MRI [13, 14], allowing for a detailed assessment of strain and stress distributions in the left ventricle (LV). To accurately replicate cardiac biomechanics in these models, it is essential to incorporate the in vivo biomechanical properties of the human myocardium with high precision.

Although the FE method and cardiac MRI are well-established tools in cardiac modeling, the novelty of our work lies in the integration

*Corresponding author:** Mohamed Deriche, Artificial Intelligence Research Centre, Ajman University, United Arab Emirates. Email: m.deriche@ajman.ac.ae

strategy and modeling choices specifically tailored to simulate the mechanical behavior of MI. Unlike previous studies that focus primarily on healthy myocardium or apply simplified boundary conditions, our approach leverages patient-specific MRI-derived geometries combined with a regionally differentiated mechanical model that distinguishes infarcted, border-zone (transitional), and healthy myocardial tissue.

Moreover, we simulate active myocardial contraction using a thermal strain-based approach, which enables a physiologically realistic representation of systolic function without relying on complex active tension models. The inclusion of fiber orientation further accounts for the anisotropic properties of myocardial tissue, enhancing the physiological fidelity of the model. These methodological advancements make our framework particularly well suited for analyzing and predicting the biomechanical consequences of MI and hold promise for future applications in diagnosis and treatment planning.

A concise summary of the main contributions of the research is presented below:

1) Development of a patient-specific FE model: A detailed FE model of the LV was constructed using cardiac MRI data from both MI patients and healthy controls. The model incorporates personalized LV geometry, infarct localization via LGE, and anisotropic myocardial properties to simulate heart-specific mechanics.
2) Clinically applicable computational framework: A novel framework was introduced, which integrates cardiac MRI with biomechanical modeling to noninvasively assess myocardial stiffness and contractility, especially in infarcted regions.
3) Enhanced characterization of infarct mechanics: The approach provides a robust and reliable method to quantify infarct-induced mechanical changes, supporting disease monitoring, early risk assessment, and tailored treatment strategies.
4) Computational efficiency and scalability: The model uses simplified yet physiologically valid assumptions (e.g., thermal strain to mimic contraction) for efficient strain simulation, making it feasible and attractive for clinical adoption and large-scale studies.

The remainder of this paper is organized as follows. The literature review is described in Section 2. The functionality of the framework is described in Section 3. The testing surroundings are also covered in Section 3. The performance outcomes of both the current and suggested frameworks are presented in Section 4. The conclusion of this paper is described in Section 5.

2. Related Works

Various researchers have conducted studies by employing computational modeling to assist physicians and reduce subjective decisions in cardiovascular diagnosis [15–19]. Genet et al. [15] focused on understanding the distribution of myofiber stress in the LV during end-diastole (ED) and end-systole (ES), intending to inform the design of heart failure treatments using computational modeling. The main idea of the study revolved around investigating the myofiber stress patterns in a normal human heart to provide insights that can guide the development of targeted treatments for heart failure. The results demonstrated distinct stress patterns between ED and ES, with higher stress concentrations observed in specific regions of the ventricular wall. Furthermore, Al-Ani and Deriche [16] developed a dynamic model of LV function using the immersed boundary method and Lagrangian FE method for describing both geometry and local features from clinical images and using an orthotropic constitutive model for passive elasticity, which allowed the quantification of local stress and strain throughout the cardiac cycle. Despite the simplifications introduced into the models, they predicted detailed displacement and strain distributions that were generally in agreement with CMR measurements

and previous clinical studies. Additionally, in 2018, a research study reported by Wang et al. [17] presented a biomechanical model of the LV by combining cardiac MRI data and hemodynamic data determined by cardiac catheterization. Using computational modeling techniques, a 3D FE model of the time-varying LV geometry was aligned with the cardiac MRI data. The proposed method showed that the ED myofiber strain in the middle ventricle was significantly higher in patients with acute heart failure than in controls and that diastolic myocardial stiffness was significantly higher in patients with reduced ejection fraction (EF) than in patients with preserved EF and controls. Recently, Rumindo et al. [18] conducted a study to estimate subject-specific myocardial stiffness and contractility in healthy individuals. They achieved this by constructing LV models from data obtained through cardiac MRI acquisition. The modeling approach was extensively validated by comparing measured or estimated local circumferential strain with other measures of global LV function. The prognostic significance of these indices needs to be further explored through longitudinal clinical studies. Recent efforts in disease modeling, including the spatio-temporal prediction of COVID-19 prevalence and mortality using artificial neural networks [19], have underscored the potential of data-driven approaches to capture complex disease dynamics. In the context of cardiac modeling, previous studies reported by Genet et al. [15], Al-Ani and Deriche [16], and Rumindo et al. [18] have primarily focused on healthy cohorts, utilizing either idealized or patient-specific geometries to assess myocardial stress, strain, and stiffness under normative physiological conditions. Despite these advances, results could still be improved. Thus, our study addresses a critical research gap by focusing specifically on MI, incorporating MRI-based infarct geometry and tissue alterations to model the pathological behavior of the LV.

3. Proposed Methodology

This section presents the proposed method for developing a computational model of a human LV. The process is structured into the following three main steps: 1) cardiac MRI data acquisition, 2) model simulation, and 3) validation, as illustrated in Figure 1.

3.1. Study subjects

In this study, cardiac MRI datasets were acquired from 20 healthy controls (4 females and 16 males; age range = 23–74 years) with no history of cardiovascular diseases and from 20 patients (3 females and 17 males; age range = 23–70 years) who had an MI. The image datasets were acquired using two MRI machines (Siemens Medical Solution, Erlangen, Germany) with electrocardiographic gating (ECG): one at the Principal Military Hospital of Instruction of Tunis, Tunisia, and the other at the Pitié Salpêtrière University Hospital, France. The local ethics committee approved the study with a waiver of informed consent.

3.2. Image acquisition and LV reconstruction

LV endocardial and epicardial contours were semi-automatically segmented using the CVI42 software (Circle Cardiovascular Imaging) at the ES and ED phases in both short- and long-axis cine images. The functional characteristics of the LV, including ES and ED volumes, EF, and stroke volume (SV), as well as the geometric characteristics, such as ED wall thickness and fractional wall thickening, were automatically calculated from the segmented LV contours. Then, the segmented contours at ES were processed with CATIA V5 (Dassault Systems) to reconstruct the LV surfaces. Finally, the obtained geometry was meshed with hexahedral elements in Abaqus FE software (Dassault Systems) (Figure 2).

Figure 1
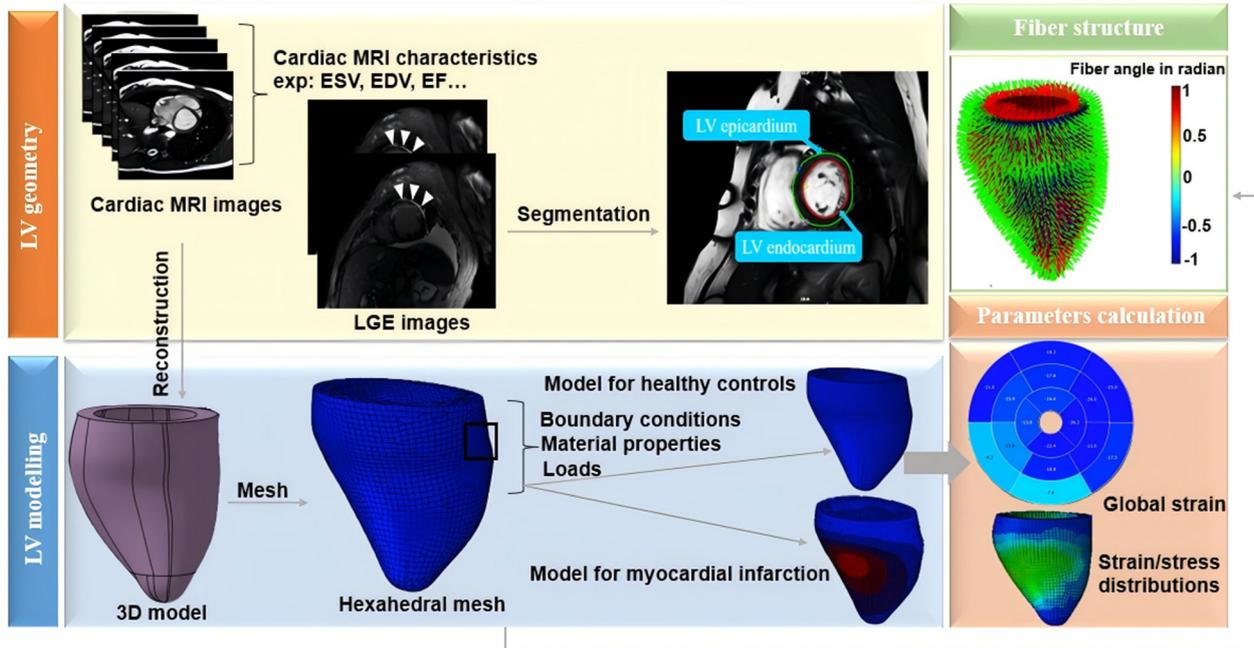**Proposed method workflow for FE LV modeling**

Figure 2
LV reconstruction from cardiac MRI: (a) cardiac MRI images (short and long axes) at ES, (b) myocardium segmentation using a semi-automatic method, and (c) final meshed LV geometry at ES
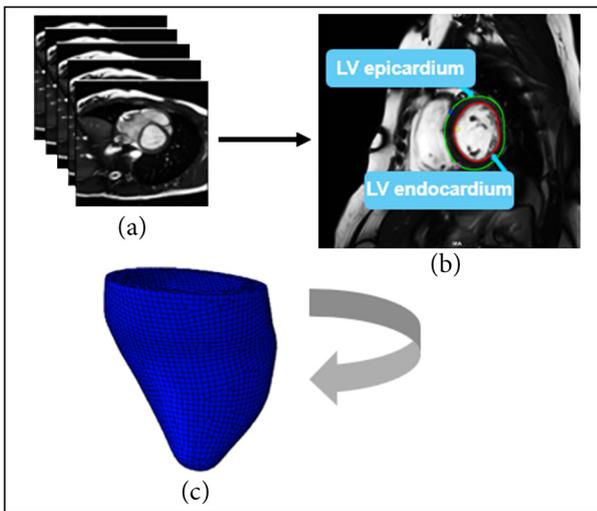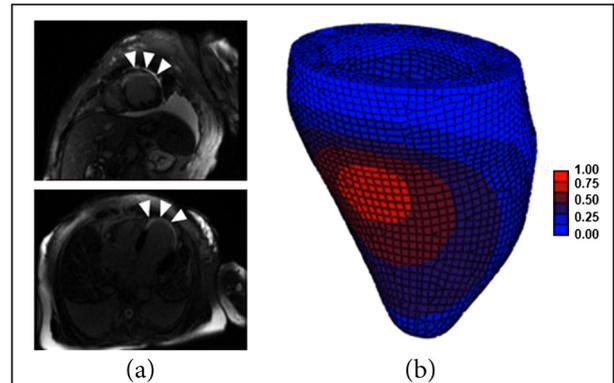

Figure 3
LV model built for an MI patient: (a) LGE short- and long-axis images at ES and (b) LV reconstruction outlined in color to represent transition regions

Note: 0: healthy myocardium, 1: the core of the infarcted myocardium

For the MI model, the infarcted region was defined by combining short-axis and long-axis LGE images with reconstructed LV geometry at ES. To ensure no change in material behavior transition from a damaged infarcted region to a healthy region, three transition regions were successively identified at a 10 mm distance from the border of the infarct [16]. Figure 3 displays LGE short- and long-axis images and the corresponding MI model.

3.3. Myocardial fiber structure

A rule-based fiber orientation was incorporated to identify the mechanical properties of the myocardium. The wall of the LV contains two layers, namely, the epicardium and endocardium. The epicardium is the outer layer, and the endocardium is the inner layer. The myocardial fiber structure was assigned using the Laplace–Dirichlet-Region growing-FEM algorithm. According to Palit et al. [20] and Wong and Kuhl [21], the helix or fiber angle varies from an endocardial +60° angle to an epicardial −60° angle relative to the basal slice. Figure 4 shows the orientation of the fibers assigned to the myocardium. There are three orthonormal axes: the fiber (f), sheetlet-normal (n), and sheetlet (s) axes. The fiber angle (α) refers to the angle that is formed between the local circumferential direction (u_c) and the projection of the fiber axe (f) on a plane perpendicular to a local radial direction (u_n). An additional important angle is the sheetlet angle (β), which represents the angle between the local radial direction (u_n) and sheetlet axe in a single element (Figure 4(a)). The Laplace–Dirichlet-Region growing-FEM algorithm required three inputs: the LV mesh geometry, a cloud of points in a plane parallel to the short-axis slice orientation directly

Figure 4

(a) Fiber (f), sheetlet-normal (n), and sheetlet (s) material axes in black; local circumferential (uc), local radial (un), and local longitudinal (uz) directions in cyan; (b) fiber orientation in the LV model with transmural distribution of fiber angle (α); and (c) the arrows in red and green indicate (f) and (s) orientations, respectively
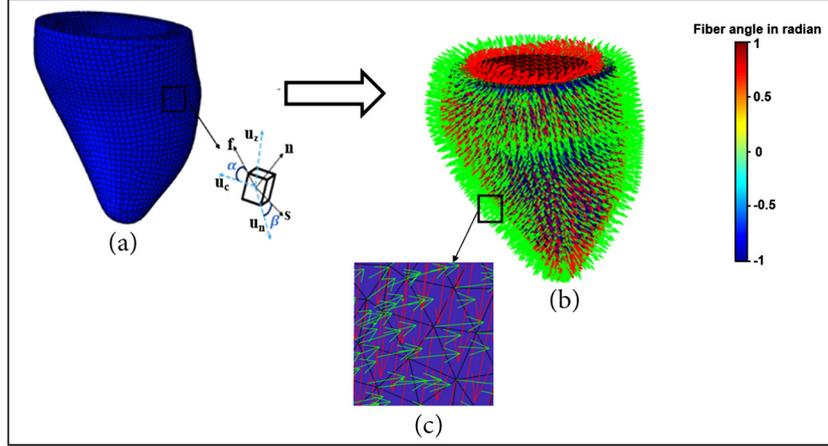
under the basal nodes' intersection, and the definition of fiber angles from histological data. The fiber orientation results of the LV geometry with the color map angle in radian are shown in Figure 4(b).

3.4. Proposed FE LV modeling

The FE method was chosen to determine the mechanical LV response of each subject, caused by pressure and volume variations during the cardiac cycle. In the present study, the ES geometry was used to model the LV because it offers useful information regarding cardiac function and can boost the assessment of its performance. This phase is important as it reflects to the minimal volume applied to the LV myocardial wall and reflects its contractile capacity [22–24]. A passive transversely anisotropic Fung-type law composed of four parameters, namely, C_0, b_f, b_t, and b_{ft}, that details the degree of nonlinearity and anisotropy in the systolic mechanical properties of the myocardial tissue is introduced by Guccione et al. [25].

$$\Psi(E) = \frac{C_0}{2}\left(e^Q - 1\right),\qquad(1)$$

with

$$\begin{aligned}\underline{Q} &= b_f\underline{E}_{ff}{}^2 + b_t\left(\underline{E}_{ss}{}^2 + \underline{E}_{nn}{}^2 + \underline{E}_{sn}{}^2 + \underline{E}_{ns}{}^2\right)\\&+ b_{ft}\left(\underline{E}_{fs}{}^2 + \underline{E}_{sf}{}^2 + \underline{E}_{fn}{}^2 + \underline{E}_{nf}{}^2\right),\end{aligned}\qquad(2)$$

where C_0 is the passive linear parameter to be identified for each subject, $\underline{Q}$ is the quadratic function of three principal strain components, b_f and $\overline{b}_t$ represent stiffness at the local myocardial fiber and at the transversal direction, respectively, and b_{ft} is shear rigidity. The ratios between parameters b_f, b_t, and b_{ft} were set to 1.0, 0.4, and 0.7, respectively, consistent with the findings of Wenk et al. [26], where $b_t = 0.4 \ b_f$ and $b_{ft} = 0.7 \ b_f$. Using this approach, the number of material parameters to be identified is reduced to two: C_0 and b_f. $\underline{E}$ indicates the Green–Lagrange strain tensor, where the subscripts f, n, and s and denote the myofiber, sheet-normal, and sheet directions, respectively.

The following initial material parameters were replicated by Rumindo et al. [18], where C_0 was set to 0.08 kPa and b_f, b_t, and b_{ft} were set to 16.15, 6.46, and 11.31, respectively. In the LV MI model, the passive material behavior was modeled by changing the material properties in the infarcted region. It was supposed that the passive

parameter (C_0) in the infarcted region increased 50 times more than that in the normal myocardium, and the transition region was defined to have normal passive properties, as suggested in previous studies [22, 26–28]. Specifically, there was no variation between the infarcted and healthy regions in the LV parameters of passive materials (b_f, b_t, and b_{ft}) [28]. The Fung-type material law was implemented using the user material in FE solver Abaqus. Our study focused on the passive properties of the myocardium. We recognize the importance of incorporating an active stress or strain component to accurately simulate myocardial contraction. To achieve this, we employed an active strain model using a thermal strain tensor. An active strain implemented by a thermal strain tensor in Abaqus can be simply described as follows [28]:

$$\varepsilon = \alpha.\Delta T,\qquad(3)$$

where α is the thermal expansion coefficient and ΔT is the temperature difference. The thermal expansion coefficient in the fiber direction was adjusted to $\alpha_{ff} = -0.32$, and the thermal expansion coefficient in the normal sheetlet and sheetlet directions was adjusted to $\alpha_{nn} = \alpha_{ss} = 0.21$ to maintain near incompressibility of the myocardial tissue. These values are based on previous studies reported by Fan et al. [28] and empirical adjustments to reflect the mechanical properties of cardiac muscle fibers. The negative sign indicates contraction in the direction of the fibers, which corresponds to the physiological shortening of myocardial fibers during systole. The active material's contractility in the infarcted region was suppressed by setting the thermal strain expansion coefficient to zero. In the transition region between healthy and infarcted tissue, normal passive properties were retained, and contractility was reduced by 50%, inspired by Fan et al. [28]. The passive parameters were identified by minimizing the deviation from the ES pressure–volume relationship (EDPVR) curve, as predicted by the formulation of Klotz et al. [29]. The Nelder–Mead optimization algorithm was used, available in Matlab (MathWorks) [30], a two-loop optimization process, inspired by the approach of Genet et al. [15].

The outer loop focused on optimizing b_f by minimizing the deviation from the Klotz curve, which represents the standard EDPVR. At each iteration of this outer loop, an inner loop was executed to adjust C_0 for the given b_f. The cost function for diastolic personalization was defined as the sum of squared errors between the normalized real volumes (MRI measured) and the simulated volumes, evaluated over a pressure range from 0 to 20 mmHg. With no subject-specific pressure data available, standardized ED and ES pressure values of 9

and 120 mmHg, respectively, were applied, as recommended by Genet et al. [15], Al-Ani and Deriche [16], Wang et al. [17], and Rumindo et al. [18]. The surface of the epicardium was homogeneous Neumann boundary conditions, and the endocardium surface was subjected to a uniform LV pressure. The basal line has been fixed to take account of the significantly higher stiffness of the annulus compared with the myocardium. This fixed basal constraint eliminates any rigid body motion, thus ensuring the stability of the simulation. We have implemented a two-point simulation in our model (two steps), applying pressure at two distinct points: ES pressure was set to 120 mmHg and ED pressure was set to 9 mmHg for healthy subjects and to 16 mmHg for patients with MI because ED pressure in patients with MI was higher than that in healthy subjects, applied on the endocardial surface [18]. Basal nodes were positioned longitudinally, and the endocardium annulus was fixed [28]. The stress in the myocardium was simulated using Abaqus. The computational model incorporates EDV and ESV derived from MRI images, and we utilized data from cardiac MRI acquisitions to reconstruct the LV geometry.

3.5. Model validation

The accuracy of the developed model was validated by comparing simulated LV volumes with those obtained from cardiac MRI data. In addition to volume validation, we compared the circumferential strain values, measured using feature tracking (FT) on cine MR images and interpolated on the FE mesh using a combination of nearest neighbor and inverse-distance-weighting (IDW) methods for comparison with the personalized simulation strains. We focused on global circumferential strain as it provides the most consistent and reliable data for comparison. Previous studies have shown that the global radial strain derived from the FT technique has a low correlation with other methods for measuring LV strain and is less robust and reproducible

[31–33]. Longitudinal strain was not included in the comparison due to the acquisition of only two long-axis images, which was insufficient for reliable analysis.

The cardiac MRI-FT analysis was processed using two software: CVI42 and CardioTrack (Sorbonne University), developed on Matlab (MathWorks) [34]. Using CVI42, endocardium and epicardium contours were identified in the whole cardiac cycle for short- and long-axis slices. Both global circumferential strain (GCS) and global radial strain (GRS) were analyzed in the short-axis slices (basal, mid ventricular, and apical). Global longitudinal strain (GLS) was assessed in three long-axis slices (2-chamber, 3-chamber, and 4-chamber).

Statistical analyses were performed using SPSS software (version 16.0, IBM SPSS Inc., USA). Statistical tests were considered statistically relevant with a p-value less than 0.05. Distribution tests were performed on all data, and continuous variables were assigned a mean ± standard deviation (SD). The dataset's characteristics and cardiac MRI metrics were tested using Student's t-test.

4. Simulated and Experimental Results

To validate the proposed model, we conducted extensive experiments and simulation studies, which are detailed in the subsections below.

4.1. Clinical and cardiac MRI subjects' characteristics

In Table 1, we present a description of the dataset used and its characteristics, as well the corresponding cardiac MRI functional and geometric metrics. No significant variation was observed in gender, age, body mass index, and heart rate between the MI patients and controls. We note that the average heart rate was higher in MI patients than in controls, although such a difference did not reach statistical

Table 1
Characteristics and cardiac MRI measures of the MI patients studied and healthy controls

Variable	Healthy controls (n = 20)	Patients with MI (n = 20)	p-value
Clinical characteristics			
Gender (male/female)	16/4	17/3	
Age (year)	48 [23–74]	52 [23–70]	0.176
BMI (kg/m2)	25.65 ± 3.20	26.60 ± 4.08	0.425
HR (beat/minute)	69.05 ± 9.33	75.45 ± 10.73	0.06
Cardiac MRI characteristics of LV			
Functional			
ESV (ml)	54.80 ± 12.72	99.00 ± 26.52	<0.001
EDV (ml)	144.00 ± 20.37	185.80 ± 36.26	0.001
SV (ml)	89.30 ± 11.76	86.70 ± 23.63	0.067
EF (%)	63.10 ± 4.24	45.75 ± 10.07	<0.001
Geometric			
ED wall thickness_basal (mm)	7.57 ± 1.71	8.78 ± 1.96	0.040
ED wall thickness_medial (mm)	6.79 ± 1.22	8.47 ± 2.15	<0.001
ED wall thickness_apical (mm)	5.68 ± 1.24	7.47 ± 1.76	<0.001
Fractional wall thickening_basal (%)	65 ± 14	41 ± 11	<0.001
Fractional wall thickening_medial (%)	67 ± 11	41 ± 14	<0.001
Fractional wall thickening_apical (%)	71 ± 14	35 ± 12	<0.001

Note: BMI: body mass index; HR: heart rate; MRI: magnetic resonance imaging; LV: left ventricle; ESV: end-systolic volume; EDV: end-diastolic volume; SV: stroke volume; EF: ejection fraction; ED: end-diastole

significance. However, important differences were noted in volumetric LV parameters (ESV and EDV), with significantly higher values in MI patients than in healthy controls. Although the EF was significantly lower in MI patients (all p < 0.001), a slight variation was found between healthy controls and patients with MI in terms of SV (p = 0.067).

Using the studied dataset, the ED wall thickness and fractional wall thickening, from the basal to apical level of the LV, were computed for healthy controls and patients with MI (Table 1). Regarding the ED wall thickness, the mean normal values for healthy controls were 7.57 ± 1.71 mm for basal slices, 6.79 ± 1.22 mm for mid-LV slices, and 5.68 ± 1.24 mm for apical slices. For patients with MI, the average normal values were 8.78 ± 1.96 mm (basal), 8.47 ± 2.15 mm (mid-LV), and 7.47 ± 1.76 mm (apical). The average values of fractional wall thickening of healthy controls were 65% ± 14% (basal slices), 67% ± 11% (mid-LV slices), and 71% ± 14% (apical slices). For MI subjects, the fractional wall thickening values were 41% ± 11% (basal), 41% ± 14% (mid-LV), and 35% ± 12% (apical) (all p < 0.05).

4.2. Simulated volumes for investigating mechanical behavior

The LV volumes simulated by the developed models were compared with the LV volumes obtained from the cardiac MRI data (Table 2). On average, the simulated volumes and those obtained from cardiac MRI ES data were equal to 55.59 ± 12.39 ml vs. 54.80 ± 12.72 ml for healthy subjects and 102.00 ± 25.99 ml vs. 99.00 ± 26.52 ml for patients with MI, respectively. The mean ED volumes simulated by the built models compared to those obtained from cardiac MRI for the healthy subjects were 151.32 ± 22.04 ml vs. 144 ± 20.37 ml and 191.13 ± 36.30 ml vs. 185.80 ± 38.26 ml for patients with MI, respectively. Both ES and ED simulated volumes closely aligned with those obtained from the cardiac MRI. The difference in LV volumes was within the range 3%–5%.

4.3. Global strain analysis

The LV global strains, namely, GCS, GLS, and GRS, derived from the built models and FT techniques in patients with MI were considerably lower than those in healthy controls. All p-values were lower than 0.001 (Table 3). The average global circumferential strains calculated for the two categories using the built models were −17.5% ± 1.1% and −11.2% ± 1.9%, respectively, and those obtained by the CVI42 software were −18.7% ± 1.9% and −12.0% ± 3.2% respectively.

The global circumferential strains computed using the CardioTrack software were −19.2% ± 1.9% for healthy subjects and −13.4% ± 3.2% for patients with MI. The average global longitudinal strains computed by both software for the healthy controls were in the same range: −17.5% ± 1.3% (CVI42) and −18.9% ± 2.3% (CardioTrack). Global radial strain was impaired in patients with MI compared with healthy controls (18% ± 5.6% vs. 32.3% ± 5.6% by CVI 42 and 43.4% ± 3% vs. 62.8% ± 11.6% by CardioTrack). Global radial strain was impaired in patients with MI compared with healthy controls (18% ± 5.6% vs. 32.3% ± 5.6% by CVI 42 and 43.4% ± 3% vs. 62.8% ± 11.6% by CardioTrack). Additionally, receiver operating characteristic curve (ROC curve) analysis was used to compare each method and to assess strain parameters' capacity to differentiate patients with MI from healthy controls (Table 4). Figure 5 illustrates the ROC curve of the global circumferential strain results obtained with the proposed method, CVI42, and CardioTrack with area under the curve (AUC) of each method.

4.4. Subject-specific passive material parameters

Table 5 presents the passive material parameters identified for each subject, as well as the mean values and the standard deviation. The table clearly demonstrates a distinction in the passive parameter (C_0) between healthy subjects and patients with MI. The mean (C_0) value for healthy myocardium is 0.088 kPa, and in the infarcted region, it increases to 6.094 kPa (p-value < 0.001). This significant difference supports findings from previous studies, which suggested that the passive myocardium in infarcted regions becomes approximately 50 times stiffer compared to healthy myocardium [19, 28–30]. No significant difference was observed in the LV parameters of passive materials ($b_f, b_t,$ and b_{ft}) between healthy controls and patients with MI (all p-value > 0.05).

4.5. Distributions of strain and stress

Figure 6 shows the ES stress and strain distribution in proximity to the endocardium and epicardium in both models. The average stress value was 0.073 ± 0.01 MPa (73 kPa) in the healthy model. The average systole stress was 0.082 ± 0.04 MPa (82 kPa) in the infarcted region. The average fiber strain distribution value was −0.15 ± 0.06 in the healthy model and 0.2 ± 0.04 in the infarcted region. The distribution of stress at ES was characterized by a nonuniform pattern. The highest stress values were observed near the subendocardial layer. In the MI model, the stress distribution was altered due to the presence of the infarcted region.

Table 2
ES and ED simulated volumes and those obtained from cardiac MRI

	ESV_CMR (ml)	ESV_Finite Element (ml)	% variation	EDV_CMR (ml)	EDV_Finite Element (ml)	% variation
Healthy subjects	54.80 ± 12.72	55.59 ± 12.39	2	144.00 ± 20.37	151.32 ± 22.04	5
Patients with MI	99.00 ± 26.52	102.00 ± 25.99	3	185.80 ± 38.26	191.13 ± 36.30	3

Note: ESV and EDV values are expressed as mean ± SD.

Table 3
LV myocardium global strain computed parameters

Method	Healthy controls			Patients with MI		
	GCS (%)	GLS (%)	GRS (%)	GCS (%)	GLS (%)	GRS (%)
CVI42	−18.7 ± 1.9	−17.5 ± 1.3	32.3 ± 5.6	−12.0 ± 3.1	−13.4 ± 3.2	18.0 ± 5.6
CardioTrack	−19.2 ± 1.9	−18.9 ± 2.3	62.8 ± 11.6	−13.4 ± 3.2	−12.7 ± 3.4	43.4 ± 3.4
Simulated	−17.5 ± 1.1	-	-	−11.2 ± 1.9	-	-

Table 4
ROC curve analysis for the used dataset

Variable	AUC ± SE	p-value	Sensitivity (%)	Specificity (%)
MI vs. healthy controls				
Cardiac MRI parameters of LV				
ESV	0.94 ± 0.03	<0.001	90	90
EDV	0.83 ± 0.07	<0.001	85	75
SV	0.65 ± 0.09	0.100	55	75
EF	0.98 ± 0.02	<0.001	95	90
Feature-tracking parameters				
GCS_CVI42	0.96 ± 0.03	<0.001	90	95
GCS_CardioTrack	0.94 ± 0.04	<0.001	95	85
GLS_CVI42	1 ± 0.00	<0.001	100	100
GLS_CardioTrack	0.93 ± 0.02	<0.001	85	80
Simulated parameters				
ESV	0.93 ± 0.03	<0.001	90	85
EDV	0.81 ± 0.07	0.001	90	70
Stress	0.84 ± 0.06	<0.001	75	70
GCS	1 ± 0.00	<0.001	100	100

Table 5
Estimated passive material parameters for healthy subjects and patients with MI

Healthy					Myocardial infarction				
Subject	C_0 (KPa)	b_f	b_t	b_f	Patient	C_0	b_f	b_t	b_{ft}
1	0.123	10.72	4.29	7.51	1	7.081	12.51	5.00	8.76
2	0.095	14.67	5.87	10.27	2	5.873	15.35	6.14	10.75
3	0.103	14.50	5.80	10.15	3	6.421	13.74	5.50	9.62
4	0.074	17.08	6.83	11.96	4	5.493	17.12	6.85	11.98
5	0.106	14.19	5.68	9.93	5	6.721	12.12	4.85	8.48
6	0.085	17.52	7.01	12.26	6	6.423	10.51	4.20	7.36
7	0.069	13.44	5.38	9.41	7	7.264	11.08	4.43	7.76
8	0.071	12.78	5.11	8.95	8	6.280	17.88	7.15	12.52
9	0.065	16.73	6.69	11.71	9	6.241	15.38	6.15	10.77
10	0.072	18.15	7.26	12.70	10	5.643	17.46	6.98	12.22
11	0.076	12.57	5.03	8.80	11	5.868	15.75	6.30	11.02
12	0.089	16.94	6.78	11.86	12	7.113	13.00	5.20	9.10
13	0.064	14.14	5.66	9.90	13	5.152	11.20	4.48	7.84
14	0.072	17.82	7.13	12.47	14	6.564	16.75	6.70	11.73
15	0.128	15.29	6.12	10.70	15	5.552	18.79	7.52	13.15
16	0.110	18.58	7.43	13.01	16	5.821	13.40	5.36	9.38
17	0.095	12.40	4.96	8.68	17	6.770	15.16	6.06	10.61
18	0.081	15.00	6.00	10.50	18	6.624	16.24	6.50	11.37
19	0.074	18.30	7.32	12.81	19	4.127	17.15	6.86	12.00
20	0.119	16.43	6.57	11.50	20	4.840	13.87	5.55	9.71
Mean	0.088	15.36	6.15	10.75	Mean	6.094	14.72	5.89	10.31
SD	0.019	2.28	0.91	1.59	SD	0.807	2.47	0.99	1.73

Table 6
Studies providing normal and pathological cardiac MRI-FT LV strain measurements

Study	Healthy controls Mean ± SD			Patients with MI Mean ± SD		
	GCS (%)	GLS (%)	GRS (%)	GCS (%)	GLS (%)	GRS (%)
Morton et al. [35]	−17.4 ± 4.0	−20.5 ± 5.0	20.8 ± 6.0	-	-	-
Augustine et al. [36]	−21.0 ± 3.0	−19.0 ± 3.0	25.0 ± 6.0	-	-	-
Genet et al. [15]	−17.6 ± 5.8	−13.9 ± 2.9	-	-	-	-
Taylor et al. [37]	−26.1 ± 4.0	−21.3 ± 5.0	39.8 ± 8.0	-	-	-
Yu et al. [38]	−20.8 ± 2.8	−15.5 ± 2.7	38.5 ± 9.3	−16.9 ± 2.2	−13.1 ± 2.2	28.4 ± 5.1
Qu et al. [39]	−17.0 ± 2.7	−15.4 ± 2.3	44.4 ± 13.0	-	-	-
Wang et al. [40]	−19.3 ± 0.0	−13.5 ± 2.6	39.6 ± 0.0	−14.7 ± 0.0	−8.9 ± 2.3	24.1 ± 0.0
Polacin et al. [41]	−19.9 ± 2.0	−18.9 ± 4.0	39.8 ± 6.0	−10.7 ± 5.0	−10.7 ± 5.0	27.9 ± 5.0
Our study, 2025	−18.7 ± 1.9	−17.5 ± 1.3	32.3 ± 5.6	−11.9 ± 3.1	−13.38 ± 3.2	17.9 ± 5.6

Figure 5
ROC curves for simulated, CVI 42, and CardioTrack global circumferential strains
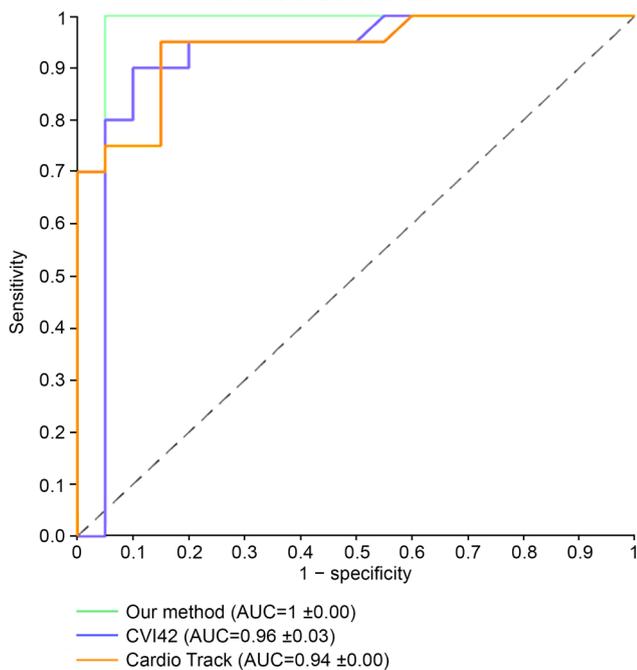
The infarcted region is often stiffer than the healthy myocardium and leads to areas of elevated stress around the infarcted zone. A positive value of strain in the infarcted region is a result of the altered or decreased normal contractile function. The global strain values obtained using the proposed method and those analyzed by cardiac MRI-FT software show a considerable variation in GCS and GLS strains when comparing patients with MI to healthy controls. However, a difference was observed in GRS derived from the two software. This significant difference could be explained by the fact that CardioTrack is based on contour detection whereas the other software uses the intra-myocardial structure to calculate the radial myocardial strain. According to Table 4, the cardiac LV parameters derived from MRI, namely, ESV, EDV, and EF, indicated a good performance, with the respective average AUCs of 0.98, 0.88, and 0.98. Similarly, average AUCs of 0.93, 0.81, and 0.84

were obtained with the simulated LV parameters: ESV, EDV, and stress. The outcomes of this study demonstrate that CVI42 and the proposed method show a slight increase in performance than the CardioTrack software in the circumferential direction (proposed method AUC: 1 and GCS_CVI42 AUC: 0.85 vs. GCS_CardioTrack AUC: 0.94). The Bland–Altman plots illustrated in Figure 7 and the average AUC values presented in Table 4 reveal a subtle distinction in strain analysis software in the range of inter-operator variability and equal differences between patients and healthy controls. Such a difference is related to technical differences in implementation. Indeed, CVI42 and CardioTrack software utilize the FT technique. However, differences may exist as one of the techniques is mainly contours-based and the other is intra-myocardial-based.

5. Discussion

This study used the FE method and measurements from cardiac MRI acquisition to estimate mechanical parameters in healthy controls and patients with MI. The potential of cardiac strain and stress analysis in detecting cardiac abnormalities, prognosis, guiding therapy, and patient follow-up was demonstrated. Accordingly, the changes found in terms of strain magnitude are more likely due to the presence of MI [42]. Patients with MI exhibited lower LV global strain values, obtained using the cardiac MRI-FT software and the proposed method, than those derived from healthy controls. ES stress and strain distributions are relatively homogenous due to the underlying myocardium structure throughout the wall [16, 17]. Compared with the healthy model, these parameters in the infarcted LV model are more pronounced in the infarcted region. These significant variations have also been demonstrated by Guccione et al. [25]. They utilized an FE model to explore the transmural distribution of fiber stress across the canine LV, providing valuable data on the variations in stress from the apex to the base. In contrast, our study refines this investigation by applying a static model to human LV data, enabling a more focused comparison of stress and strain in both healthy and infarcted myocardial regions. Furthermore, ES stress and strain distribution results correlated well with those in previous studies. As an example, in a study by Al-Ani and Deriche et al. [16], where the authors computed models of LV under healthy and pathological conditions using cardiac MRI images of a healthy subject and a patient with MI, the stress distribution values were 64 ± 19 kPa and 65 ± 32 kPa in the healthy model and in the infarcted region, respectively. Similarly, in the study by Wong and Kuhl [21], the fiber strain distribution values were −0.19 ± 0.04 and 0.02 ± 0.02

Figure 6
Simulation results of healthy and infarcted LV models regarding the fiber stress and strain distributions near the myocardium
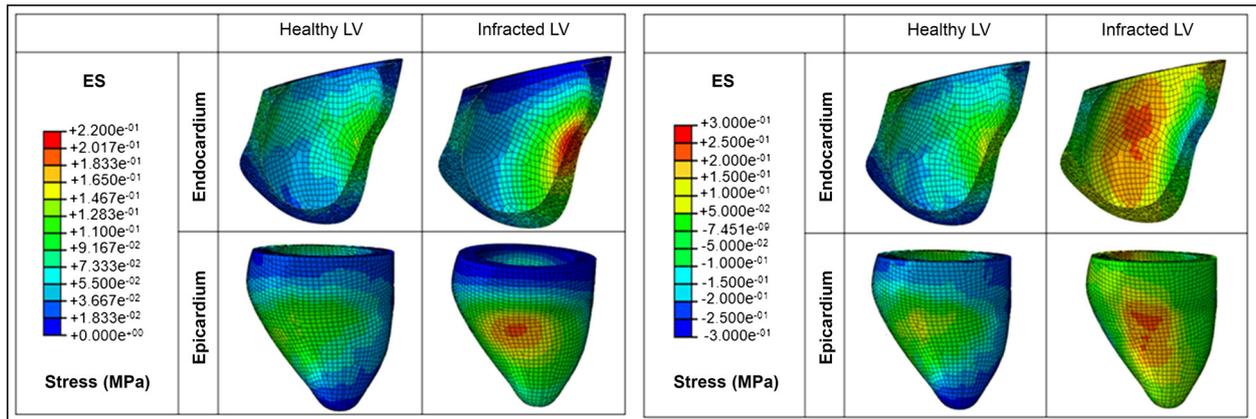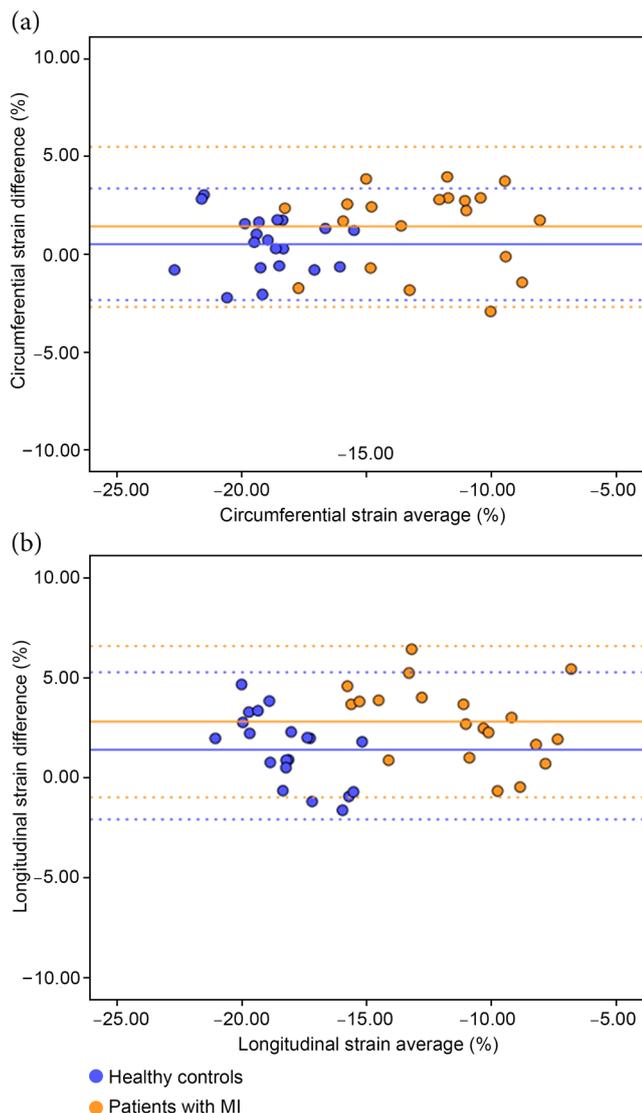

Figure 7
Bland–Altman plots for strain quantification methods CVI42 and CardioTrack for each group of subjects' (a) circumferential strain and (b) longitudinal strain

in the healthy model and in the infarcted region, respectively, which correlates well with the overall average of -0.15 ± 0.06 for the healthy model and 0.2 ± 0.04 for the infarcted region found in the current study. In literature, several state-of-the-art studies [15, 35–41] that use the FT technique for LV strain measurements also utilize the same imaging modalities, cardiac MRI, as this study but with a variable number of subjects (Table 6).

Although the proposed method yields promising results, several limitations should be acknowledged. First, the use of a simplified FE model may introduce biases in estimating regional mechanical behavior. Specifically, the assignment of uniform material properties to infarcted and peri-infarcted regions may lead to underestimation or overestimation of local stress and strain, particularly in areas exhibiting significant tissue heterogeneity. Second, the model does not account for multiphysical interactions such as electrical conduction, hemodynamics, and metabolic activity, all of which are critical to cardiac function and remodeling. The omission of these physiological processes may hinder the model's ability to capture the intricate coupling between mechanical and biological responses. Third, the study is based on a relatively small dataset, potentially limiting the generalizability and robustness of the findings. The significant results of this study encourage one to consider expanding the used dataset and exploring the potential of artificial intelligence (AI) and machine learning in future research projects. AI could be employed to refine parameter estimation, enabling more precise personalization of the model based on patient-specific data. For example, it could be used to analyze large datasets from MRI or other imaging modalities to optimize the mechanical properties of the myocardium in both healthy and infarcted regions [43, 44].

6. Conclusion

In this work, an FE model was developed using cardiac MRI data to simulate LV stress and strain distributions at ES for both healthy individuals and MI patients. The model included data from 40 subjects and enabled the estimation of GCS, GLS, and GRS. These strain measurements were then compared with those obtained via the FT technique. The results demonstrated strong correlation, highlighting the capability of the proposed method to accurately capture myocardial deformation. Notably, the strain patterns derived from the model showed significant potential in distinguishing between healthy and infarcted myocardium. The findings suggest that this FE-based approach could serve as a valuable diagnostic tool for assessing myocardial viability and improving clinical decision-making in cardiac care.

Conflicts of Interest

The authors declare that they have no conflicts of interest to this work.

Data Availability Statement

Data are available from the corresponding author upon reasonable request.

Author Contribution Statement

Rania Awadi: Conceptualization, Methodology, Software, Validation, Formal analysis, Investigation, Data curation, Writing – original draft, Writing – review & editing, Visualization. **Narjes Benameur:** Methodology, Validation, Investigation, Writing – review & editing, Visualization, Supervision, Project administration. **Wafa Baccouch:** Formal analysis, Writing – review & editing, Visualization. **Mohamed Deriche:** Methodology, Writing – review & editing, Visualization, Project administration, Funding acquisition. **Arnab Palit:** Validation, Visualization. **Moncef Aloui:** Resources, Data curation. **Nadjia Kachenoura:** Software, Validation, Resources, Data curation, Writing – review & editing, Visualization. **Salam Labidi:** Methodology, Investigation, Writing – review & editing, Visualization, Supervision, Project administration.

References

[1] Coronado, F., Melvin, S. C., Bell, R. A., & Zhao, G. (2022). Global responses to prevent, manage, and control cardiovascular diseases. *Preventing Chronic Disease*, *19*, 220347. http://dx.doi.org/10.5888/pcd19.220347

[2] World Health Organization. (2021). *Global health estimates: Leading causes of death—Cause-specific mortality, 2000–2021*. https://www.who.int/data/gho/data/themes/mortality-and-global-health-estimates/ghe-leading-causes-of-death

[3] Awadi, R., Benameur, N., Kraiem, T., & Salam, L. (2023). A quasi-static biomechanical model of the human myocardium based on cardiac magnetic resonance images. *Procedia Computer Science*, *219*, 1177–1184. https://doi.org/10.1016/j.procs.2023.01.399

[4] Dali, M., Benameur, N., & Labidi, S. (2023). A new approach for native myocardial T1 mapping using a standard single-shot MRI pulse sequence technique. *Procedia Computer Science*, *219*, 1216–1223. https://doi.org/10.1016/j.procs.2023.01.404

[5] de Luca, L., Colivicchi, F., Gabrielli, D., Lucci, D., Grippo, G., Piemonte, F., …, & Gulizia, M. M. (2022). Incidence, characteristics, and management of patients with recurrent myocardial infarctions: Insights from the EYESHOT POST-MI. *Journal of Interventional Cardiology*, *2022*(1), 4593325. https://doi.org/10.1155/2022/4593325

[6] Garza, M. A., Wason, E. A., & Zhang, J. Q. (2015). Cardiac remodeling and physical training post myocardial infarction. *World Journal of Cardiology*, *7*(2), 52–64. https://dx.doi.org/10.4330/wjc.v7.i2.52

[7] Yi, L., Zhu, T., Qu, X., Buayiximu, K., Feng, S., Zhu, Z., …, & Yan, X. (2024). Predictive value of early left ventricular end-diastolic volume changes for late left ventricular remodeling after ST-elevation myocardial infarction. *Cardiology Journal*, *31*(3), 451–460. https://doi.org/10.5603/cj.90492

[8] Baccouch, W., Hasnaoui, B., Benameur, N., Jemai, A., Lahidheb, D., & Labidi, S. (2025). Deep learning-based algorithm for the classification of left ventricle segments by hypertrophy severity. *Journal of Imaging*, *11*(7), 244. https://doi.org/10.3390/jimaging11070244

[9] Benameur, N., Caiani, E. G., Arous, Y., Ben Abdallah, N., & Kraiem, T. (2018). Parametric imaging for the assessment of cardiac motion: A review. *Cardiovascular Engineering and Technology*, *9*(3), 377–393. https://doi.org/10.1007/s13239-018-0362-1

[10] Grautoff, S., Fessele, K., Fandler, M., Knappen, N., & Gotthardt, P. (2023). „STEMI mimics": ST-hebungen im EKG: Alternative diagnosen zum akuten koronarverschluss [„STEMI mimics": ST elevations on ECG: Alternative diagnoses to acute coronary occlusion]. *Medizinische Klinik - Intensivmedizin und Notfallmedizin*, *118*(1), 35–44. https://doi.org/10.1007/s00063-021-00882-5

[11] Beijnink, C. W. H., van der Hoeven, N. W., Konijnenberg, L. S. F., Kim, R. J., Bekkers, S. C. A. M., Kloner, R. A., …, & Nijveldt, R. (2021). Cardiac MRI to visualize myocardial damage after ST-segment elevation myocardial infarction: A review of its histologic validation. *Radiology*, *301*(1), 4–18. https://doi.org/10.1148/radiol.2021204265

[12] Zhao, X., Zhang, L., Wang, L., Zhang, W., Song, Y., Zhao, X., & Li, Y. (2025). Magnetic resonance imaging quantification of left ventricular mechanical dispersion and scar heterogeneity optimize risk stratification after myocardial infarction. *BMC Cardiovascular Disorders*, *25*(1), 2. https://doi.org/10.1186/s12872-024-04451-4

[13] Mondal, S., & Ghosh, R. (2020). Experimental and finite element investigation of total ankle replacement: A review of literature and recommendations. *Journal of Orthopaedics*, *18*, 41–49. https://doi.org/10.1016/j.jor.2019.09.019

[14] Mondal, S., MacManus, D. B., Bonatti, A. F., de Maria, C., Dalgarno, K., Chatzinikolaidou, M., …, & Dunne, N. (2023). A computational analysis of a novel therapeutic approach combining an advanced medicinal therapeutic device and a fracture fixation assembly for the treatment of osteoporotic fractures: Effects of physiological loading, interface conditions, and fracture fixation materials. *Medical Engineering & Physics*, *114*, 103967. https://doi.org/10.1016/j.medengphy.2023.103967

[15] Genet, M., Lee, L. C., Nguyen, R., Haraldsson, H., Acevedo-Bolton, G., Zhang, Z., …, & Guccione, J. M. (2014). Distribution of normal human left ventricular myofiber stress at end diastole and end systole: A target for in silico design of heart failure treatments. *Journal of Applied Physiology*, *117*(2), 142–152. https://doi.org/10.1152/japplphysiol.00255.2014

[16] Al-Ani, A., & Deriche, M. (2002). Feature selection using a mutual information based measure. In *2002 International Conference on Pattern Recognition*, *4*, 82–85. https://doi.org/10.1109/ICPR.2002.1047405

[17] Wang, Z. J., Wang, V. Y., Bradley, C. P., Nash, M. P., Young, A. A., & Cao, J. J. (2018). Left ventricular diastolic myocardial stiffness and end-diastolic myofibre stress in human heart failure using personalised biomechanical analysis. *Journal of Cardiovascular Translational Research*, *11*(4), 346–356. https://doi.org/10.1007/s12265-018-9816-y

[18] Rumindo, G. K., Ohayon, J., Croisille, P., & Clarysse, P. (2020). In vivo estimation of normal left ventricular stiffness and contractility based on routine cine MR acquisition. *Medical Engineering & Physics*, *85*, 16–26. https://doi.org/10.1016/j.medengphy.2020.09.003

[19] Kianfar, N., Mesgari, M. S., Mollalo, A., & Kaveh, M. (2022). Spatio-temporal modeling of COVID-19 prevalence and mortality using artificial neural network algorithms. *Spatial and Spatio-Temporal Epidemiology*, *40*, 100471. https://doi.org/10.1016/j.sste.2021.100471

[20] Palit, A., Bhudia, S. K., Arvanitis, T. N., Turley, G. A., & Williams, M. A. (2015). Computational modelling of left-ventricular diastolic mechanics: Effect of fibre orientation and right-ventricle topology. *Journal of Biomechanics*, *48*(4), 604–612. https://doi.org/10.1016/j.jbiomech.2014.12.054

[21] Wong, J., & Kuhl, E. (2014). Generating fibre orientation maps in human heart models using Poisson interpolation. *Computer Methods in Biomechanics and Biomedical Engineering*, *17*(11), 1217–1226. https://doi.org/10.1080/10255842.2012.739167

[22] Shavik, S. M., Wall, S., Sundnes, J., Guccione, J. M., Sengupta, P., Solomon, S. D., …, & Lee, L. C. (2021). Computational modeling studies of the roles of left ventricular geometry, afterload, and muscle contractility on myocardial strains in heart failure with preserved ejection fraction. *Journal of Cardiovascular Translational Research*, *14*(6), 1131–1145. https://doi.org/10.1007/s12265-021-10130-y

[23] Cicci, L., Fresca, S., Manzoni, A., & Quarteroni, A. (2024). Efficient approximation of cardiac mechanics through reduced-order modeling with deep learning-based operator approximation. *International Journal for Numerical Methods in Biomedical Engineering*, *40*(1), e3783. https://doi.org/10.1002/cnm.3783

[24] Franco, P., Sotelo, J., Montalba, C., Ruijsink, B., Kerfoot, E., Nordsletten, D., …, & Uribe, S. (2021). Comprehensive assessment of left intraventricular hemodynamics using a finite element method: An application to dilated cardiomyopathy patients. *Applied Sciences*, *11*(23), 11165. https://doi.org/10.3390/app112311165

[25] Guccione, J. M., Costa, K. D., & McCulloch, A. D. (1995). Finite element stress analysis of left ventricular mechanics in the beating dog heart. *Journal of Biomechanics*, *28*(10), 1167–1177. https://doi.org/10.1016/0021-9290(94)00174-3

[26] Wenk, J. F., Sun, K., Zhang, Z., Soleimani, M., Ge, L., Saloner, D., …, & Guccione, J. M. (2011). Regional left ventricular myocardial contractility and stress in a finite element model of posterobasal myocardial infarction. *Journal of Biomechanical Engineering*, *133*(4), 044501. https://doi.org/10.1115/1.4003438

[27] Amin, A., & Deriche, M. (2016). Salt-dome detection using a codebook-based learning model. *IEEE Geoscience and Remote Sensing Letters*, *13*(11), 1636–1640. https://doi.org/10.1109/LGRS.2016.2599435

[28] Fan, Y., Ronan, W., & Teh, I. (2019). A comparison of two quasi-static computational models for assessment of intra-myocardial injection as a therapeutic strategy for heart failure. *International Journal for Numerical Methods in Biomedical Engineering*, *35*(9), e3213. https://doi.org/10.1002/cnm.3213

[29] Klotz, S., Hay, I., Dickstein, M. L., Yi, G.-H., Wang, J., Maurer, M. S., …, & Burkhoff, D. (2006). Single-beat estimation of end-diastolic pressure-volume relationship: A novel method with potential for noninvasive application. *American Journal of Physiology-Heart and Circulatory Physiology*, *291*(1), H403–H412. https://doi.org/10.1152/ajpheart.01240.2005

[30] Lagarias, J. C., Reeds, J. A., Wright, M. H., & Wright, P. E. (1998). Convergence properties of the Nelder–Mead simplex method in low dimensions. *SIAM Journal on Optimization*, *9*(1), 112–147. https://doi.org/10.1137/S1052623496303470

[31] Militaru, S., Panovsky, R., Hanet, V., Amzulescu, M. S., Langet, H., Pisciotti, M. M., …, & Gerber, B. L. (2021). Multivendor comparison of global and regional 2D cardiovascular magnetic resonance feature tracking strains vs tissue tagging at 3T. *Journal of Cardiovascular Magnetic Resonance*, *23*(1), 54. https://doi.org/10.1186/s12968-021-00742-3

[32] Lim, C., Blaszczyk, E., Riazy, L., Wiesemann, S., Schüler, J., von Knobelsdorff-Brenkenhoff, F., & Schulz-Menger, J. (2021). Quantification of myocardial strain assessed by cardiovascular magnetic resonance feature tracking in healthy subjects—Influence of segmentation and analysis software. *European Radiology*, *31*(6), 3962–3972. https://doi.org/10.1007/s00330-020-07539-5

[33] Brandt, Y., Lubrecht, J. M., Adriaans, B. P., Aben, J., Gerretsen, S. C., Ghossein-Doha, C., …, & Kooi, M. E. (2024). Quantification of left ventricular myocardial strain: Comparison between MRI tagging, MRI feature tracking, and ultrasound speckle tracking. *NMR in Biomedicine*, *37*(9), e5164. https://doi.org/10.1002/nbm.5164

[34] Lamy, J., Soulat, G., Evin, M., Huber, A., de Cesare, A., Giron, A., …, & Kachenoura, N. (2018). Scan–rescan reproducibility of ventricular and atrial MRI feature tracking strain. *Computers in Biology and Medicine*, *92*, 197–203. https://doi.org/10.1016/j.compbiomed.2017.11.015

[35] Morton, G., Schuster, A., Jogiya, R., Kutty, S., Beerbaum, P., & Nagel, E. (2012). Inter-study reproducibility of cardiovascular magnetic resonance myocardial feature tracking. *Journal of Cardiovascular Magnetic Resonance*, *14*(1), 34. https://doi.org/10.1186/1532-429X-14-43

[36] Augustine, D., Lewandowski, A. J., Lazdam, M., Rai, A., Francis, J., Myerson, S., …, & Leeson, P. (2013). Global and regional left ventricular myocardial deformation measures by magnetic resonance feature tracking in healthy volunteers: Comparison with tagging and relevance of gender. *Journal of Cardiovascular Magnetic Resonance*, *15*(1), 8. https://doi.org/10.1186/1532-429X-15-8

[37] Taylor, R. J., Moody, W. E., Umar, F., Edwards, N. C., Taylor, T. J., Stegemann, B., …, & Leyva, F. (2015). Myocardial strain measurement with feature-tracking cardiovascular magnetic resonance: Normal values. *European Heart Journal – Cardiovascular Imaging*, *16*(8), 871–881. https://doi.org/10.1093/ehjci/jev006

[38] Yu, S., Zhou, J., Yang, K., Chen, X., Zheng, Y., Zhao, K., …, & Zhao, S. (2021). Correlation of myocardial strain and late gadolinium enhancement by cardiac magnetic resonance after a first anterior ST-segment elevation myocardial infarction. *Frontiers in Cardiovascular Medicine*, *8*, 705487. https://doi.org/10.3389/fcvm.2021.705487

[39] Qu, Y.-Y., Paul, J., Li, H., Ma, G.-S., Buckert, D., & Rasche, V. (2021). Left ventricular myocardial strain quantification with two- and three-dimensional cardiovascular magnetic resonance based tissue tracking. *Quantitative Imaging in Medicine and Surgery*, *11*(4), 1421–1436. https://doi.org/10.21037/qims-20-635

[40] Wang, Q., Wang, J., Ma, Y., Wang, P., Li, Y., Tian, J., …, & Li, B. (2022). Predictive value of myocardial strain on myocardial infarction size by cardiac magnetic resonance imaging in ST-segment elevation myocardial infarction with preserved left ventricular ejection fraction. *Frontiers in Pharmacology*, *13*, 1015390. https://doi.org/10.3389/fphar.2022.1015390

[41] Polacin, M., Karolyi, M., Eberhard, M., Matziris, I., Alkadhi, H., Kozerke, S., & Manka, R. (2022). Segmental strain for scar detection in acute myocardial infarcts and in follow-up exams using non-contrast CMR cine sequences. *BMC Cardiovascular Disorders*, *22*(1), 226. https://doi.org/10.1186/s12872-022-02664-z

[42] Yang, W., Xu, J., Zhu, L., Zhang, Q., Wang, Y., Zhao, S., & Lu, M. (2024). Myocardial strain measurements derived from MR feature-tracking: Influence of sex, age, field strength, and vendor. *JACC: Cardiovascular Imaging*, *17*(4), 364–379. https://doi.org/10.1016/j.jcmg.2023.05.019

[43] Zingaro, A., Bucelli, M., Piersanti, R., Regazzoni, F., Dede', L., & Quarteroni, A. (2024). An electromechanics-driven fluid dynamics model for the simulation of the whole human heart. *Journal of Computational Physics*, *504*, 112885. https://doi.org/10.1016/j.jcp.2024.112885

[44] Olsen, C. R., Mentz, R. J., Anstrom, K. J., Page, D., & Patel, P. A. (2020). Clinical applications of machine learning in the diagnosis, classification, and prediction of heart failure. *American Heart Journal*, *229*, 1–17. https://doi.org/10.1016/j.ahj.2020.07.009